LANGMUIR

Photocatalytic Degradation of Organic Pollutants by Sulfate Radicals Activated by Defective NH$_2$-MIL-88B

Zeping Qin, Mingming Sun, Runjie Wu, Pengkun Li, Ran Tai, Hongfei Su, John Tressel, Bicheng Ji, Qiang Wang,* and Shaowei Chen*

Read Online

ACCESS | Metrics & More | Article Recommendations | Supporting Information

ABSTRACT: Photocatalysis has been recognized as a viable technology for pollutant degradation in wastewater, owing to its ability to generate reactive radicals under photoirradiation. Among these, sulfate radicals (SO_4^-) have been attracting significant attention due to their strong oxidizing properties; yet the specific mechanism of action has remained elusive thus far. In this study, defective NH$_2$-MIL-88B (DNMB) is prepared via a facile hydrothermal procedure in the presence of potassium sodium tartrate and found to facilitate the production of sulfate radicals from sulfate anions under visible light irradiation, due to partial reduction of Fe^{3+} to Fe^{2+} in the NMB skeleton by the added tartrate that enriches the Fe^{3+}/Fe^{2+} redox couples, in addition to other reactive species like superoxide radicals and hydroxy radicals. This effectively improves the degradation efficiency toward a variety of organic pollutants, including antibiotics such as tetracycline (TC), sulfamethoxazole (SMX), and levofloxacin (LEV), as well as common organic contaminants like bisphenol A (BPA) and rhodamine B (RhB), as compared to pristine NMB. Specifically, after 40 minutes of visible light irradiation, the degradation rate increases from 61.5% to 92.1% for TC, from 76.1% to 89.4% for SMX, from 60.5% to 75.2% for LEV, from 61.7% to 91.2% for BPA, and from 78.4% to 94.8% for RhB. The primary active species are identified to be sulfate radicals, with minor contributions from holes, superoxide radicals, and hydroxyl radicals, as demonstrated in quenching experiments and electron spin resonance measurements, and further confirmed by theoretical studies. Degradation pathways for the various pollutants are then proposed based on results from Fukui index calculations and liquid chromatography−mass spectrometry analysis. These results underscore the crucial role of structural engineering in driving the advancement of green and sustainable technologies for environmental engineering.
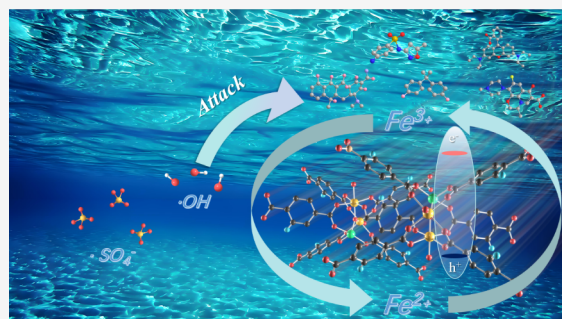
INTRODUCTION

Discharge of organic pollutants from industrial wastewater and domestic sewage has posed a significant challenge to both ecological environments and human health.[1−4] These pollutants are diverse in nature and may contain substances that exhibit high stability and low biodegradability and are difficult to eliminate by conventional water treatment methods, such as chemical oxidation and biodegradation.[5−8] As a result, development of efficient, green, and sustainable technologies for pollutant removal has become a key research focus and technical challenge in the field of environmental science and engineering.[9−13]

In recent years, photocatalysis has emerged as an attractive advanced oxidation technology toward pollutant degradation,[14−16] where the effective separation of the electron−hole pairs facilitates the photocatalytic production of holes (h$^+$), superoxide radicals (O$_2^-$), and hydroxyl radicals (●OH), among others.[17−20] Sulfate radicals (SO$_4^-$) have also garnered increasing attention due to their strong oxidizing property and high selectivity.[19,21] Thus, far, SO$_4^-$ radicals are generated

mostly from the activation of persulfate (S$_2$O$_8^{2-}$) and peroxymonosulfate (PMS, (HSO$_5^-$) ions. For example, Meng et al.[22] prepared composite catalysts based on biochar-supported cobalt single atoms, which completely degraded acetaminophen in 11 min due to effective activation of PMS by the CoN$_3$ moiety to produce SO$_4^-$. Ren et al.[23] used high-density polyethylene waste as a raw material to prepare single-atom catalysts with the FeN$_4$Cl coordination moieties dispersed within a graphene scaffold (Fe−N/Cl−C), where the axial chelation of chloride enhanced the PMS activation by the FeN$_4$ sites, leading to rapid degradation of diverse pollutants.

Nevertheless, studies of direct activation of sulfate anions (SO$_4^{2-}$) to produce SO$_4^-$ have been scarce and mostly confined

to phenomenological observations and performance validation, without systematic and in-depth analyses of the specific mechanisms of the activation process and ensuing photocatalytic degradation. In addition, the attack of SO_4^- to pollutant-specific sites, the intermediates and reaction pathways involved, as well as their synergistic effects with other reactive species have not been fully understood. This has limited the further application in practical water treatment.[21,24]

NH$_2$-MIL-88B (NMB), a typical metal−organic framework (MOF) material, has attracted widespread attention for environmental remediation, thanks to abundant active sites, good chemical and thermal stability, and large surface area. Moreover, the iron centers in NMB can participate in catalytic (Fenton) reactions through the Fe^{3+}/Fe^{2+} redox couple.[5,25,26] In this study, a defect-engineered NMB (DNMB) material was prepared hydrothermally with the addition of potassium sodium tartrate in sample synthesis and found to significantly enhance the generation of SO_4^- from SO_4^{2-}, due to partial reduction of Fe^{3+} to Fe^{2+} within the NMB skeleton by the added tartrate that enriched the Fe^{3+}/Fe^{2+} redox couples. In fact, upon the addition of sulfate ions, the degradation efficiency by DNMB toward various pollutants was significantly improved, ranging from antibiotics such as tetracycline (TC), sulfamethoxazole (SMX), and levofloxacin (LEV) to common organic contaminants like bisphenol A (BPA) and rhodamine B (RhB), as compared to NMB. In quenching and electron spin resonance (ESR) measurements, SO_4^- was identified as the major active species, with minor contributions from holes (h$^+$), superoxide radicals (O_2^-), and hydroxyl radicals ($\bullet$OH). Based on results from Fukui index calculations and liquid chromatography−mass spectrometry (LC-MS) measurements, the atomic sites of radical attacks were identified and the degradation pathways were proposed for the various contaminants.

■ EXPERIMENTAL SECTION

Chemicals. The chemicals were all obtained from Shanghai Maclin Biochemical Co. and used as received. Water was provided with a Barnstead Nanopure Water System (resistivity 18 MΩ cm).

Synthesis of Defective NH$_2$-MIL-88B. In brief, 5 mmol of ferric chloride (FeCl$_3$·6H$_2$O), 5 mmol of 2-amino terephthalic acid, and 0.25 mmol of potassium sodium tartrate were mixed under sonication for 30 min in 25 mL of dimethylformamide (DMF). The solution was then poured into a 50 mL polytetrafluoroethylene reactor, where 2 mL of a 2 M NaOH solution was added to adjust the pH. The sealed reactor was heated in an oven for 12 h at 100 °C. Upon completion of the reaction, the precipitates were obtained by centrifugation, washed with DMF three times, and then dried at 120 °C for 12 h. The resulting product was referred to as DNMB. The control sample of NMB was synthesized in the same fashion but in the absence of potassium sodium tartrate (Table S1).

Characterization. Scanning electron microscopy (SEM) was performed using a Hitachi S-4800 microscope, while transmission electron microscopy (TEM) was conducted with an FEI-Tecnai G2 F20 instrument. X-ray diffraction (XRD) analysis was carried out using a Shimadzu XRD-6100 diffractometer with Cu K$_\alpha$ radiation. XPS characterization was performed on a Thermo Fisher Scientific ESCALAB 250 system, with spectral calibration standardized against the adventitious carbon C 1s peak (284.8 eV). ESR spectra were collected on a Bruker A300 spectrometer. Raman spectra were collected in backscattering geometry using a Horiba miniature Raman spectrometer. Fourier-transform infrared (FTIR) spectra were obtained using a Bruker Tensor II FTIR NEXUS spectrometer at room temperature in the 800−4000 cm^{-1} range. The UV−visible diffuse reflectance spectroscopy (DRS) measurements were carried

out on a Shimadzu UV-2600 spectrophotometer. Steady-state and time-resolved photoluminescence (PL) characteristics were analyzed using an Edinburgh FLS1000 fluorescence spectrometer. Electrochemical characterization was performed on a CHI 760E electrochemical workstation, and nitrogen adsorption−desorption experiments were conducted with a Micromeritics ASAP2460 analyzer to obtain isotherm data. The surface hydrophilicity of the samples was assessed using a Tantec CAM-PLUS contact angle meter.

Photocatalytic Degradation of Pollutants. In brief, 25 mg of the NMB or DNMB sample prepared above was dispersed into a pollutant solution (i.e., TC, SMX, LEV, BPA, RhB, and actual wastewater, 50 mL at 20 mg L^{-1}), along with a calculated amount of sodium sulfate (Na$_2$SO$_4$). The mixture was stirred in the dark for half an hour to reach an adsorption/desorption equilibrium before simulated sunlight irradiation (>420 nm) with a Perfect light FX300 xenon lamp (300 W, with a UV cutoff filter). Sampling was conducted at 10 min intervals by extracting 2.0 mL aliquots from the reactor, followed by centrifugation for photocatalyst removal. The resulting supernatant underwent UV−vis spectroscopic analysis, with the degradation efficiency quantified through monitoring absorbance reduction over time.

Recycling Tests. The stability and reusability of the NMB and DNMB samples was examined by executing the photocatalytic experiment over four repetitions. After each test, the photocatalysts were harvested, thoroughly washed with ethanol and water, and then dried at 60 °C prior to the subsequent test.

Photoelectrochemistry. Photoelectrochemical measurements were performed using a standard three-electrode system within a 0.1 M Na$_2$SO$_4$ electrolyte under visible-light irradiation from a 300 W xenon source. The electrochemical cell comprised a platinum wire counter electrode and a saturated calomel reference electrode (SCE). For working electrode preparation, 5 mg of the NMB or DNMB powder was ultrasonically dispersed in 1 mL ethanol for 10 min. A 0.1 mL aliquot of the homogeneous suspension was then deposited onto fluorine-doped tin oxide (FTO) glass substrates (1 cm × 2 cm) and thermally annealed at 60 °C for 12 h to ensure adhesion.

Computational Study. The Fukui function (f) has been extensively utilized in computational chemistry to identify and characterize molecular sites susceptible to electrophilic, nucleophilic, and radical attacks.[27,28] It is defined as

$$f(r) = \left(\frac{\partial^2 E}{\partial N . \partial v(r)} \right) = \left[\frac{\partial \mu}{\partial v(r)} \right]_N = \left[\frac{\partial \rho(r)}{\partial N} \right]_{V(r)} \quad (1)$$

The Fukui function formalism defines $\rho(r)$ as the spatial electron density distribution, where the system's total electron count (N) and external potential (v) are respectively encoded in the partial derivatives. For atomic-resolution analysis, this reactivity descriptor adopts condensed representations using atomic population numbers to approximate localized electron densities. Specifically, the condensed Fukui function (CFF) quantification involves three distinct reaction contexts:

$$\text{Nucleophilic attack}: f_k^+ = q_N^k - q_{N+1}^k \quad (2)$$

$$\text{Electrophilic attack}: f_k^- = q_{N-1}^k - q_N^k \quad (3)$$

$$\text{Radical attack}: f_k^0 = (q_{N-1}^k - q_{N+1}^k)/2 \quad (4)$$

In the electronic state descriptor framework, q^k quantifies the localized electronic charge distribution at atomic site k. Whereas the Fukui index establishes comparative reactivity profiles across molecular domains, elevated CFF magnitudes correlate strongly with nucleophilic susceptibility. Given the predominance of SO_4^- radicals as the dominant oxidative agent, the radical-attack-specific CFF formalism (eq 4) served as the principal metric for evaluating pollutant degradation pathways, with particular emphasis on site-specific reaction probabilities.
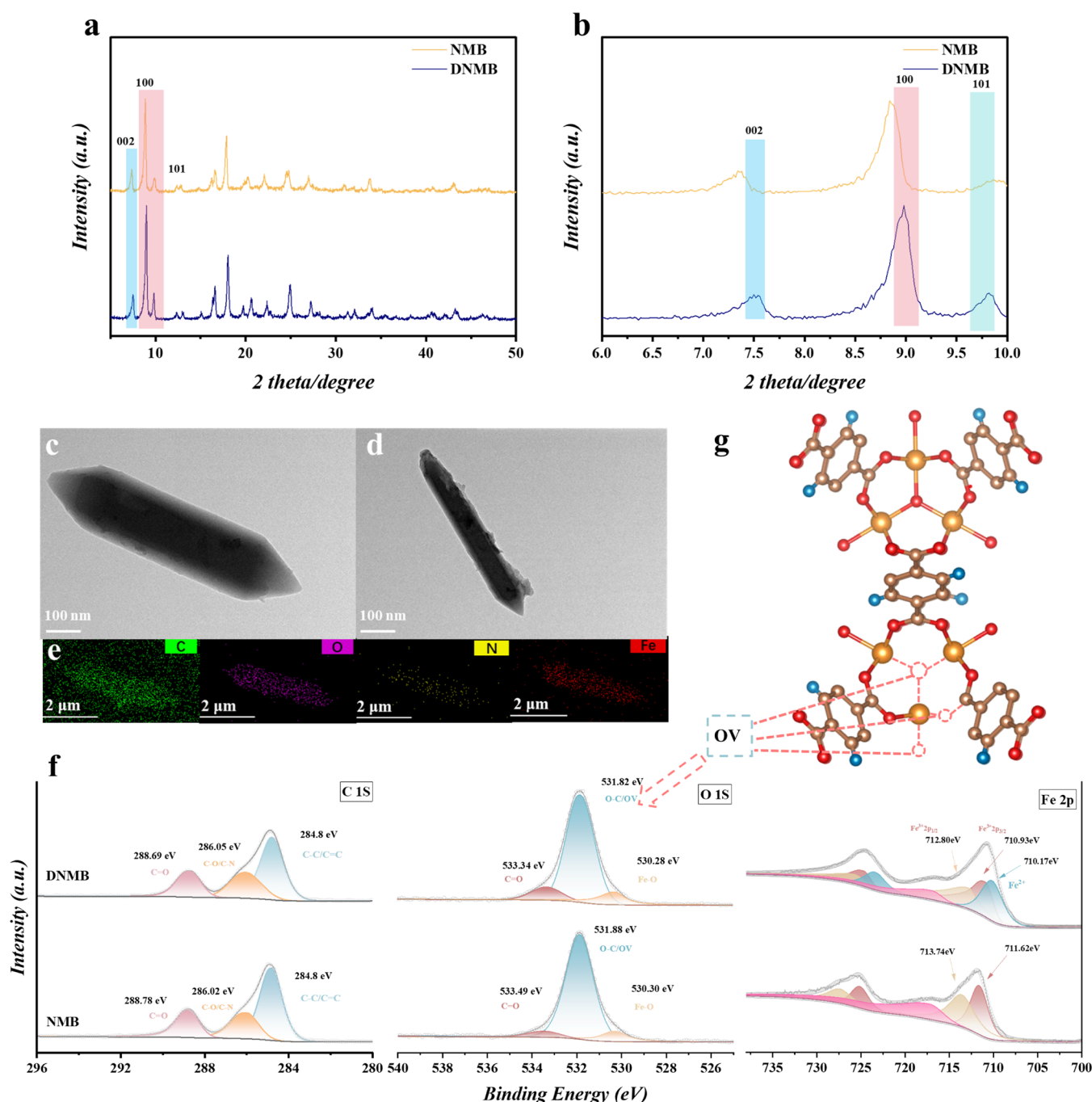
Figure 1. (a) XRD patterns of NMB and DNMB, with the range of 6° to 10° zoomed in in (b). TEM images of (c) NMB and (d) DNMB. Scale bars are both 100 nm. (e) EDS-based elemental maps of NMB. Scale bar 2 μm. (f) High-resolution XPS scans of the C 1s, O 1s and Fe 2p electrons of NMB and DNMB. (g) Schematic illustration of oxygen vacancy in NMB.

◼ RESULTS AND DISCUSSION

Structural Features. The structures of the samples obtained were first probed by XRD measurements. From Figure 1a-b, NMB can be observed to exhibit three diffraction peaks at 2θ = 7.3°, 8.8°, and 9.9° that can be ascribed to the NMB (100), (002), and (101) crystal planes, respectively.[10] DNMB displayed similar XRD patterns, but the (002) and (100) peaks can be seen to shift to a slightly higher diffraction angle at 7.5° and 9.0°, and the (101) peak to a lower diffraction angle at 9.8°, suggesting expansion of the NMB lattices most likely due to the formation of structural defects as the sample was synthesized in the presence of potassium

sodium tartrate. This is in good coincidence with a growth of the specific surface area, pore diameter, and pore volume, as manifested in nitrogen sorption measurements (Table S2, vide infra).[29]

Indeed in TEM measurements (Figures 1c,d and S1a,b), NMB can be seen to display a smooth, elongated spindle morphology, while the addition of potassium sodium tartrate led to a roughened surface of the DNMB sample, consistent with an increase of the surface area and crystal damage.[30] This morphological variation is also manifested in SEM measurements (Figure S1c,d), with a slight increase of the sample size from ca. 0.55 μm for NMB to 0.78 μm for DNMB (Figure S2).
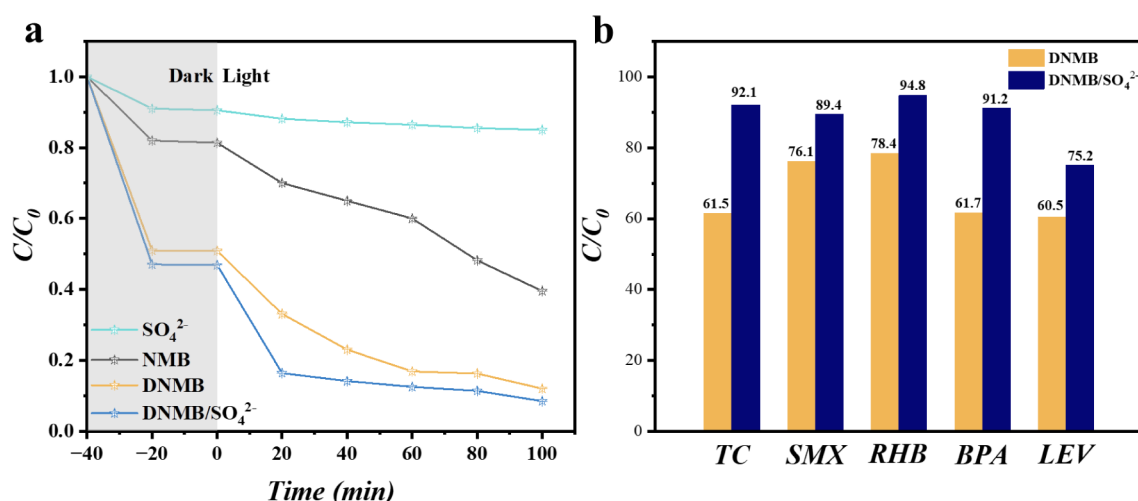
Figure 2. (a) Photocatalytic degradation of TC by NMB, DNMB, SO_4^{2-}, and $DNMB/SO_4^{2-}$. SO_4^{2-} concentration 10 mg L^{-1} (pH = 7). (b) Comparison of the corresponding degradation performance of $DNMB/SO_4^{2-}$ toward various pollutants after 40 min's visible light irradiation (TC, BPA, RHB, SMX, and LEV).

Elemental mapping via energy-dispersive X-ray spectroscopy (EDS) further demonstrated homogeneous spatial distributions of Fe, O, C, and N across the NMB specimen, as illustrated in Figure 1e.

NMB demonstrates anisotropic crystallization along the (001) crystallographic axis, with (101) facet planes dominating its surface morphology. The framework architecture features Fe^{3+} trimers bridged by carbonate ligands, where each iron center achieves pentagonal coordination through μ_3-O bridges and carboxylate (−COO−) moieties. This coordination geometry generates undercoordinated metallic vertices protruding into hexagonal nanochannels. Along these (001)-aligned unidimensional pores reside coordinatively unsaturated sites (Fe-CUS), which mediate anion-dependent charge transfer dynamics and interfacial hydration processes (Figure 1g).[31] Crucially, the thermally activated Fe^{3+}/Fe^{2+} redox couples at these CUS loci constitute catalytically active domains for surface-mediated reactions.

XPS analysis systematically probed the valence states and elemental signatures of NMB/DNMB systems. Survey spectra (Figure S3) confirm characteristic core-level emissions: C 1s (~284 eV), O 1s (~530 eV), and Fe 2p (~711 eV) align with literature benchmarks.[5,32] High-resolution deconvolution reveals three carbonaceous configurations in both materials Figure 1f (**left**): graphitic C=C (284.80 eV), heteroatom-bonded C−N/O (286.02 eV), and carbonyl C=O (288.69 eV). Oxygen speciation analysis (Figure 1f, **middle**) delineates three distinct states—lattice Fe−O (530.30 eV), defective O−C/oxygen vacancy (OV) (531.88 eV), and surface-adsorbed C=O (533.40 eV)—demonstrating comparable oxygen coordination environments between NMB and DNMB.[33,34] Yet the Fe 2p spectra are markedly different (Figure 1f, **right**). NMB can be seen to possess two doublets at 711.61/725.13 eV and 713.74/727.58 eV, corresponding to the Fe^{3+} $2p_{3/2}/2p_{1/2}$ electrons (the related satellite peaks can be found at 717.27 and 729.68 eV), while DNMB consisted of three doublets, 710.17/723.41 eV for Fe^{2+}, 710.93/725.05 eV and 712.80/726.03 eV for Fe^{3+}.[1] This indicates partial reduction of Fe^{3+} to Fe^{2+} during sample synthesis by the addition of potassium sodium tartrate. Also, the binding energies of the Fe^{3+} species can be seen to exhibit a small red-shift from DNMB to NMB, likely due to

enrichment of OV in the former (Figure 1g). Notably, the cycling between Fe^{2+} and Fe^{3+} can contribute to the generation of reactive species during photocatalytic degradation.[35]

ESR measurements yielded consistent results (Figure S4), where both NMB and DNMB can be seen to exhibit a spectral feature at g = 2.003, confirming the formation of OV within the samples. In addition, the peak-to-peak intensity is noticeably greater for DNMB than for NMB, indicating a significantly increased concentration of OV in the former.[36] This is in good agreement with the partial reduction of Fe^{3+} to Fe^{2+} during sample synthesis by potassium sodium tartrate, as observed in XPS measurements (Figure 1f).

OV served as catalytic accelerators for molecular oxygen adsorption-activation synergy. DFT simulations leveraged three defect configurations (O_a, O_b, O_c) to elucidate O_2 activation mechanisms (Figure S5). The O_a site correlates with coordinatively unsaturated Fe centers in pristine NMB,[37] while the O_b/O_c defect pairs—localized at Fe−O bonds in DNMB as evidenced by XPS and ESR—were systematically modeled. NMB's O_2 adsorption demonstrated an O−O bond length of 1.257 Å with a −1.0961 eV binding energy (Figure S5a). Contrastingly, DNMB's defective systems exhibited progressive O−O bond elongation (1.265 → 1.276 Å) coupled with strengthened adsorption energetics (−1.3072 → −2.3198 eV). This comparative analysis revealed that defect engineering creates thermodynamically favorable O_2 activation pathways, establishing OV-mediated adsorption as the photocatalytic rate-determining step.

The hierarchical porosity and surface accessibility were probed via N_2 physisorption analysis, capitalizing on MIL-88B's intrinsic framework adaptability that enables reversible pore modulation (termed "breathing" behavior). Both materials displayed Type III adsorption profiles with H_4 hysteresis (Figure S6), characteristic of mesoporous slit-shaped architectures. Quantitative analysis revealed DNMB's substantially improved textural parameters, exhibiting a 7-fold enhancement in specific surface area (35.05 vs 4.90 m^2 g^{-1}) and augmented total pore volume (0.24 vs 0.033 cm^3 g^{-1}) relative to NMB (Table S2).[26,38] This textural optimization correlates with defect-induced structural modifications (Figure
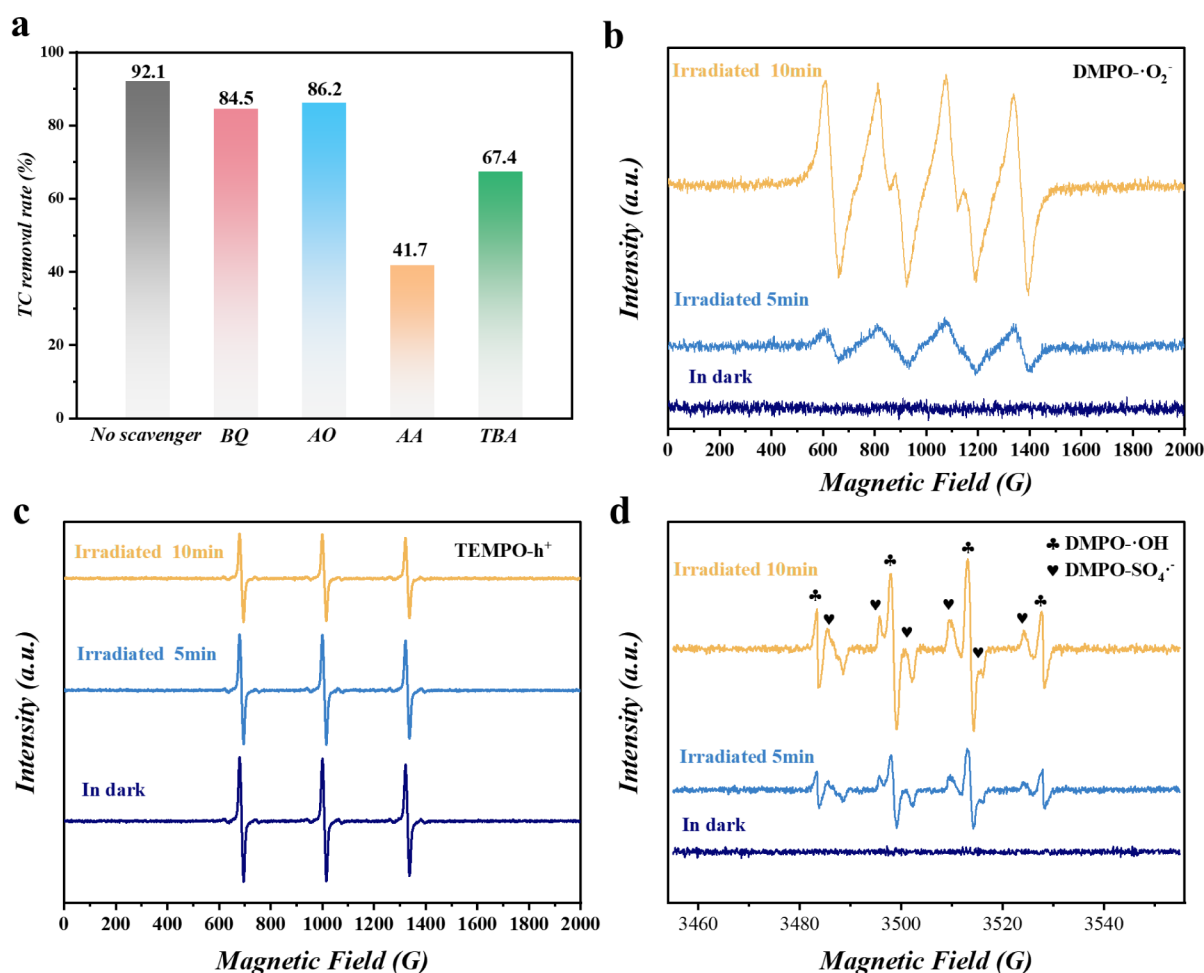
Figure 3. (a) Degradation efficiency of TC by DNMB/SO_4^{2-} without and with the addition of different scavengers. ESR spectral profiles of (b) DMPO-O_2^-, (c) TEMPO-h$^+$ and (d) DMPO-•OH/SO_4^- generated by DNMB/SO_4^{2-} after exposure to visible light for up to 10 min, in comparison to those acquired in the dark. Na_2SO_4 concentration 10 mg L^{-1} (pH = 7).

1d), establishing enhanced reactant accessibility as a critical enabler for photocatalytic efficiency amplification.

Consistent results were obtained from electrochemical studies. From the transient photocurrent response profiles (Figure S7a), DNMB can be seen to exhibit a drastically greater photocurrent density than NMB; and from the Nyquist plot of the electrochemical impedance (Figure S7b), the charge-transfer resistance (R_{CT}) was evaluated to be ca. 6.3 kΩ for NMB, and markedly lower at 4.2 kΩ for DNMB, suggesting significant enhancement of charge transport kinetics in the latter.[39]

Meanwhile, steady-state PL measurements were conducted to examine the carrier separation efficiency of the samples. As shown in Figure S8a, NMB and DNMB both exhibited an emission peak at ca. 475 nm under 380 nm photoirradiation. Yet, the peak intensity was significantly reduced for DNMB as compared to that of NMB, signifying that the recombination of photogenerated electrons and holes was drastically impeded (which was beneficial for photocatalysis).[40] At the same excitation wavelength, time-resolved PL spectra were recorded for both samples (Figure S8b), and the data were fitted with a biexponential function, where the average carrier lifetime was estimated to be 2.99 ns for NMB and prolonged markedly to 4.32 ns for DNMB (Table S3), in line with results from the above photocurrent, impedance, and PL studies.

Finally, the hydrophilic properties of the samples were tested by water contact angle experiments. From Figure S9, NMB can be seen to exhibit a water contact angle of 18.31°, in comparison to only 6.47° for DNMB. The increasing hydrophilicity of the latter is consistent with the formation of structural defects, which would facilitate the interaction between the sample and pollutants, a critical step in the photocatalytic degradation.[41]

Sulfate-Promoted Degradation of Pollutants. The degradation efficiency of TC by NMB and DNMB was first assessed and compared without and with the addition of SO_4^{2-} (10 mg L^{-1}). From Figure 2a,b, one can see that the NMB or SO_4^{2-} alone exhibited only limited degradation of TC with a degradation efficiency of ca. 61.5% and 15.7% and degradation rate constant (k) of 0.0083 and 0.0013 min^{-1} (Figure S10) after 100 min of visible light irradiation, respectively; and the degradation efficiency was drastically improved with DNMB, reaching a degradation efficiency of ca. 92.8% and k = 0.0186 min^{-1}. The performance was further enhanced with DNMB/ SO_4^{2-} (10 mg L^{-1} represented the optimal concentration of the added Na_2SO_4, Figure S11), achieving ca. 86.8% degradation at only 20 min (k = 0.0194 min^{-1}), in comparison to 69.4% for DNMB alone, indicative of the significant impacts of SO_4^{2-} on the degradation performance.
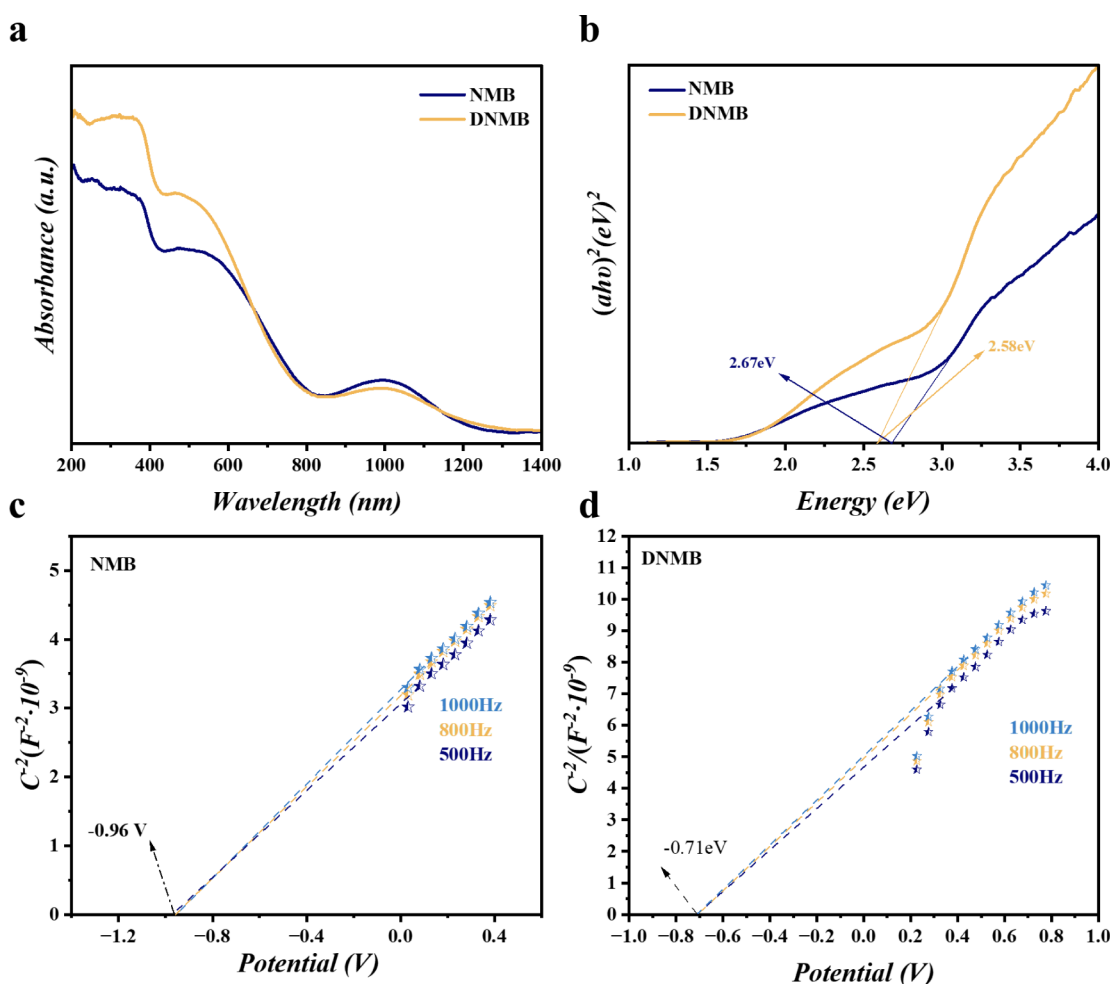
Figure 4. (a) UV−vis DRS curves and (b) the corresponding Tauc plots of NMB and DNMB. Mott−Schottky plots of (c) NMB and (d) DNMB at different frequencies.

The photocatalytic activity of DNMB/SO_4^{2-} was also markedly enhanced toward various other pollutants, as compared to DNMB alone. From Figure 2, it can be seen that after visible photoirradiation for 40 min, the removal rate increased significantly from 76.1% to 89.4% for SMX, from 60.5% to 75.2% for LEV, from 61.7% to 91.2% for BPA, and from 78.4% to 94.8% for RhB. Since the photocatalytic activity of (D)NMB relied primarily on the redox property of the Fe^{3+}/Fe^{2+} couples in the sample,[32,42] the enhanced degradation performance observed with DNMB/SO_4^{2-} was most likely due to the continuous switching of the Fe^{3+}/Fe^{2+} unsaturated coordination sites that promoted the activation of SO_4^{2-} and production of sulfate radicals.

■ REACTION MECHANISM

Determination of Active Species. Radical scavenging experiments have systematically identified reactive species in the photocatalytic system using species-specific inhibitors: ammonium oxalate (h^+), benzoquinone (O_2^-), ascorbic acid (SO_4^-), and tert-butanol ($\bullet OH$).[27,43−45] As shown in Figure 3a, the DNMB/SO_4^{2-} system's TC degradation efficiency under visible light irradiation for 100 min displayed differential scavenging responses, decreasing from 92.1% to 84.5% (BQ), 86.2% (AO), 41.7% (AA), and 67.4% (TBA). The pronounced 50.4% efficiency suppression by ascorbic acid strongly implicates sulfate radicals—generated via photoinduced SO_4^{2-} reduction—as the predominant oxidative mediators. Secondary contributions arose from superoxide radicals (8.6% inhibition), hydroxyl radicals (24.7%), and hole-mediated pathways (5.9%), collectively verifying the multimechanistic nature of the photocatalytic process.

Consistent results were obtained in ESR measurements using spin-trapping agents of 5,5-dimethyl-1-pyrroline N-oxide (DMPO) and 2,2,6,6-tetramethylpiperidine-1-oxyl (TEMPO).[46,47] It can be clearly seen that superoxide radicals ($O_2^{\cdot-}$, Figure 3b), holes (h^+, Figure 3c),[48] sulfate radicals ($SO_4^{\cdot-}$) and hydroxyl radicals ($\bullet OH$) (Figure 3d)[49,50] were readily produced by DNMB/SO_4^{2-} under visible light irradiation, and the signals became intensified with prolonged exposure to photoirradiation, in sharp contrast to the featureless profiles observed in the dark. This suggests that the photocatalytic activity toward pollutant degradation was indeed due to the synergistic contributions of these reactive species.

Degradation Mechanisms. To unravel the generation mechanisms of the aforementioned reactive species, the energy band structures of DNMB and NMB were analyzed using solid-state UV−vis spectroscopy and Mott−Schottky measurements. From Figure 4a, one can see that whereas both DNMB and NMB exhibited wide absorption bands spanning 200 to
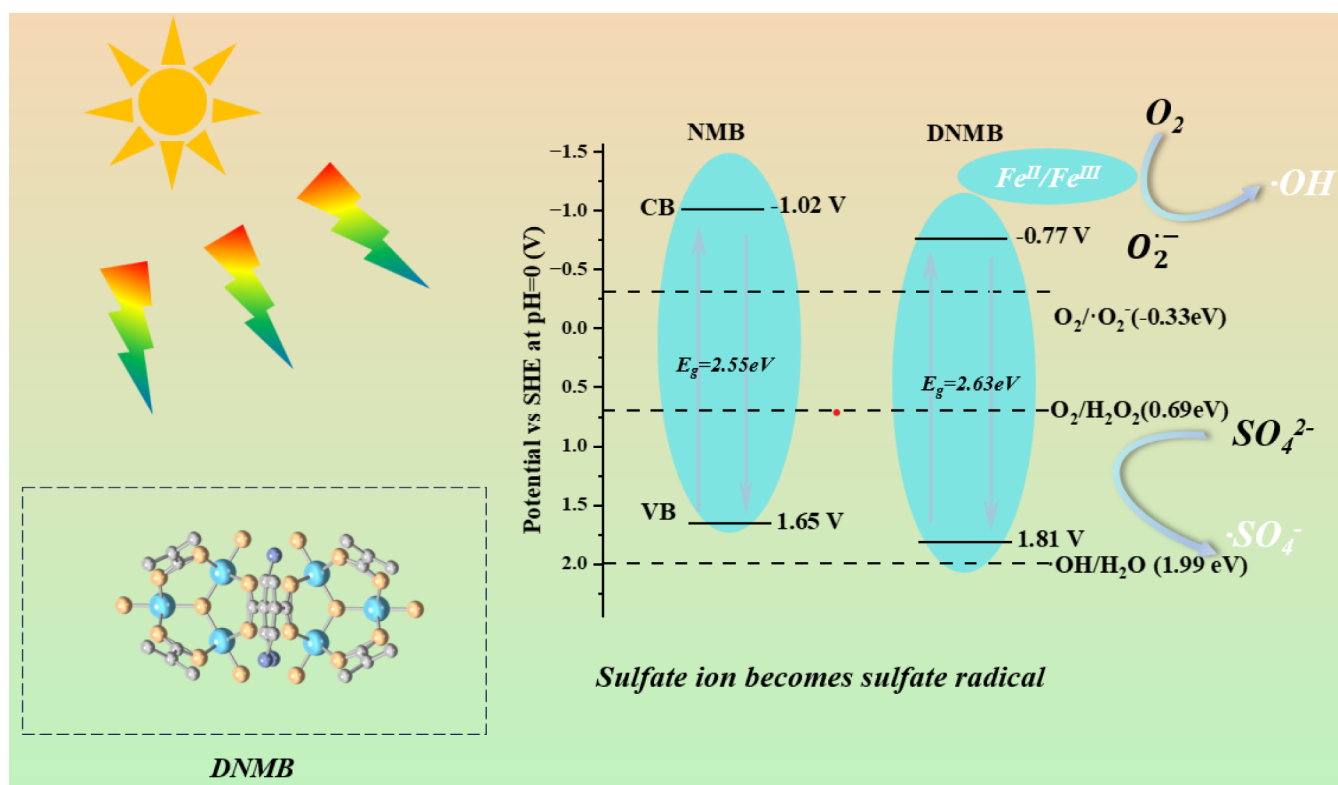
Figure 5. Band structure and reaction mechanism of the DNMB/SO_4^{2-} system.
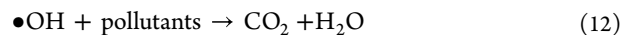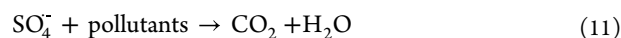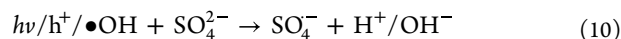
1500 nm, the DNMB sample showed enhanced absorption between 300 and 600 nm. This may be ascribed to potassium sodium tartrate added during the synthesis of DNMB, where the carboxyl functional groups of tartrate enhanced the $\pi-\pi*$ conjugation of the organic ligands in DNMB.[32,51] The prominent absorption in the visible light range was due to the Fe−O clusters and amino moieties within the organic linkers. The associated Tauc plots (Figure 4b) reveal that the bandgap was ca. 2.67 eV for NMB and somewhat lower at 2.58 eV for DNMB.

Additionally, results from Mott−Schottky measurements (Figure 4c,d) indicate that both NMB and DNMB exhibit a positive slope at various frequencies, confirming their n-type semiconductor characteristics.[36] Based on the linear regression intercepts, the flat band potential (E_{FB}) was evaluated to be −0.71 V for DNMB (vs SHE, standard hydrogen electrode) and −0.96 V for NMB (Table S4). The downshift of E_{FB} in DNMB is attributable to the enrichment of OV in the sample (which was confirmed in ESR measurements, vide infra).

The electronic band alignment and associated redox pathways in the DNMB/SO_4^{2-} system is mechanistically illustrated in Figure 5. Comparative analysis reveals that NMB exhibits conduction/valence band potentials at −1.02 V/ +1.65 V (vs SHE), while defect engineering shifts these to −0.77 V/+1.81 V for DNMB. Crucially, both materials' conduction bands surpass the thermodynamic thresholds for O_2 reduction to O_2^- (−0.33 V) and H_2O_2 generation (+0.69 V), enabling photoelectron-mediated oxygen activation through eqs 5-7. The valence band potentials, however, remain below the H_2O/●OH oxidation potential (+1.99 V), excluding direct hole-mediated hydroxyl radical formation. Instead, ESR-detected ●OH likely originates from iron-catalyzed Fenton cycling (eq 8) and secondary Haber-Weiss reactions (eqs 8-9),

as substantiated by the scavenging experiments and prior mechanistic studies.,[5,25,26]

The SO_4^- radicals were then produced either by ●OH reduction or h+ oxidation of SO_4^{2-} anions adsorbed on the DNMB surface (eq 10),[52,53] and participated in the photocatalytic degradation of the organic pollutants (eqs 11,12). The reaction mechanism can be summarized in the following steps.

$$DNMB + h\nu \rightarrow h^+ + e^- \tag{5}$$

$$O_2 + e \rightarrow O_2^- \tag{6}$$

$$O_2^- + 2H^+ \rightarrow H_2O_2 \tag{7}$$

$$H_2O_2 + Fe^{2+} \rightarrow Fe^{3+} + OH^- + \bullet OH \tag{8}$$

$$Fe^{3+} + O_2^- \rightarrow O_2 + Fe^{2+} \tag{9}$$

$$h\nu/h^+/\bullet OH + SO_4^{2-} \rightarrow SO_4^- + H^+/OH^- \tag{10}$$

$$SO_4^- + pollutants \rightarrow CO_2 + H_2O \tag{11}$$

$$\bullet OH + pollutants \rightarrow CO_2 + H_2O \tag{12}$$

Frontier molecular orbital theory and Fukui index calculations were then conducted to unravel the specific degradation pathways and reactive sites of the pollutant molecules. Figure 6a presents the HOMO and LUMO of TC which is composed of benzene rings, enol groups, and ketone groups.[54,55] Frontier orbital analysis reveals distinct electron-transfer propensities across the studied pharmaceuticals. For TC derivatives (Figure 6a), the electron-donating HOMO localizes at the C4 aromatic ring with diethylamino substituent ($N(CH_3)_2$), creating an electrophilic susceptibility hotspot for radical oxidation processes.[56] Conversely, the electron-accept-
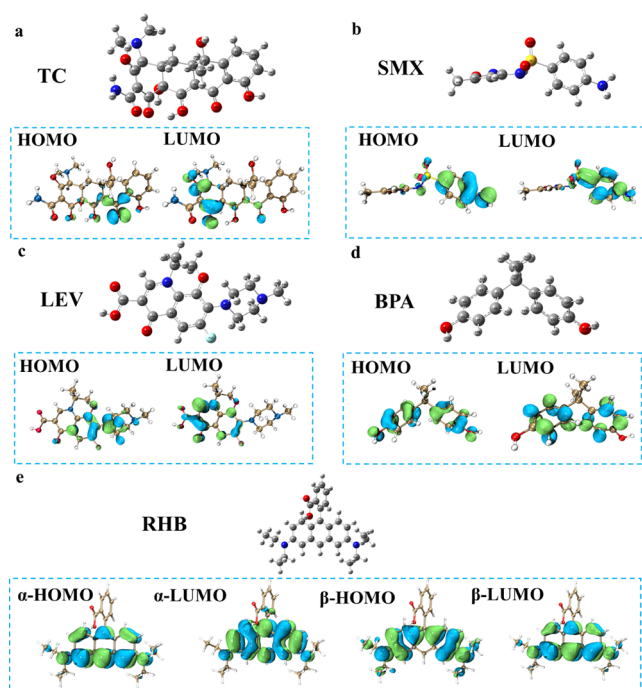
Figure 6. Frontier molecular orbital theory HOMO−LUMO for (a) TC, (b) SMX, (c) LEV, (d) BPA and (e) RhB.

ing LUMO occupies π^*-antibonding orbitals that mediate nucleophilic attack patterns. This electronic polarization dictates preferential electron depletion at the C4 pharmacophore during oxidative degradation. Comparative molecular orbital mapping shows contrasting reactivity landscapes: SMX (Figure 6b) exhibits HOMO−LUMO separation across its benzenoid system, rendering the aromatic ring susceptible to simultaneous electrophilic/nucleophilic assaults that induce π-system rupture.[2] LEV (Figure 6c) demonstrates spatial segregation of frontier orbitals-the HOMO concentrates on the fluorinated benzene moiety while the LUMO populates the quinolone core's oxazine-nitrogen heterocycle, establishing distinct sites for oxidative versus reductive transformation pathways. This indicates that these regions are more susceptible to nucleophilic attacks, primarily by sulfate radicals and hydroxyl radicals. In the case of BPA (Figure 6d), the HOMO is concentrated on the carbons of the substituted groups, while the LUMO is concentrated on the carbons of the unsubstituted groups. This suggests that substitution and elimination reactions are likely to occur at the ortho positions of the benzene ring, ultimately leading to ring-opening degradation.[57] Finally, for RhB (Figure 6e), due to its complex electronic structure, the calculations of HOMO and LUMO consider electrons in the spin-up (α) and spin-down (β) configurations, with α-HOMO and β-HOMO determined separately.[58] The results suggest that nucleophilic attacks preferentially occur at the triple bonds, with ring-opening reactions identified as the key degradation step. These findings elucidate the molecular-level mechanisms by which radicals interact with pollutants, highlighting the importance of specific functional groups and molecular sites in driving degradation pathways.

Based on the above computational results, in combination with Fukui index calculations and LC-MS results (Figures S12−S16), the possible degradation pathways of the pollutants were proposed.[59] For TC (Figure S17), the f^0 values are the

highest at C22 (0.046) and C31 (0.040), while the f^+ values are maximized at C2 (0.080) and C18 (0.077). Figure S18 illustrates the possible pathways of TC degradation, informed by the Fukui indices and intermediates identified by LC-MS measurements. Three distinct degradation trajectories emerged for TC mineralization (Figure S18). Pathway 1 initiates with hydrolytic decarboxylation generating P1−1 (401 m/z), progressing through sequential amine group elimination and structural simplification to phenolic derivatives (P1−5, 94 m/z). Parallel pathway 2 involves keto-intermediate formation (P2−1, 408 m/z; P2−2, 365 m/z) via oxidative dehydration, converging with Pathway 1 at the pivotal P1−3 (267 m/z) node. The dominant Pathway 3 exhibits branched reaction cascades: initial N-demethylation produces P3−1 (380 m/z), followed by aliphatic chain β-scission yielding P3−2. Subsequent cycloreversion events generate low-molecular-weight fragments (P3−3/4/7:262−156 m/z), which undergo oxidative defunctionalization to terminal metabolites (P3−8/9:126−112 m/z). Critical decarboxylation steps ultimately mineralize aromatic residuals into H_2O and CO_2 through radical-mediated C−C bond cleavage.[60,61]

Fukui function analysis of SMX revealed distinct reactivity hotspots, with maximal electrophilic (f^+) indices at C2 (0.0789) and C4 (0.0743), and nucleophilic (f^0) propensity at N7 (0.0758) and N13 (0.0661), as illustrated in Figure S19. Four interconnected degradation pathways were mechanistically resolved (Figure S20): (1). Hydroxylation-driven scission: SMX undergoes hydroxylation to form P1 (269 m/z) and P2 (267 m/z), followed by N−S bond cleavage yielding P3(1) (171 m/z) and P3(2) (98 m/z), which further mineralize to P4 (107 m/z) and terminal products. (2). Deamination cascade: P3(2) undergoes β-elimination at N7/N13 to generate P5 (99 m/z), progressing toward full mineralization. (3). Aromatic core decomposition: Cycloreversion of SMX produces P6 (157 m/z), which via oxidative deamination transforms into P7 (142 m/z). (4). Multistep defunctionalization: Sequential hydroxylation and ring expansion generate P8 (246 m/z), subsequently converted to P9 (218 m/z) through coupled dehydroxylation/deamination. All pathways converge via radical-mediated C−N bond cleavage and aromatic ring fragmentation.[9,62,63]

Computational analysis of LEV demonstrated that the C8 and O15 positions exhibit the highest susceptibility to radical attacks (as reflected by f^+ and f^0 values, Figure S21), with three distinct degradation pathways identified (Figure S22). Pathway 1 begins with pyrazole ring cleavage (362 m/z), forming intermediate P1 (334 m/z). This intermediate undergoes sequential defluorination and decarboxylation to yield P2 (356 m/z), while concurrent oxidation-mediated deprotonation of the carboxylic acid group generates P3 (276 m/z). Pathway 2 involves piperazine ring cleavage followed by defluorination to produce P4 (276 m/z), which is further degraded via decarboxylation and quinoline ring-opening into P5 (194 m/z). Pathway 3 initiates with piperazine ring cleavage to form P6 (321 m/z). Conversion of the tertiary amine to a secondary amine yields P7 (294 m/z), with subsequent decarboxylation and ring cleavage reactions progressively degrading the intermediate into P8 (179 m/z) and P9 (195 m/z). Extended degradation drives continuous molecular weight reduction, ultimately generating low-molecular-weight species P10−P13 (54−93 m/z). Experimental validation confirms that prolonged degradation achieves complete mineralization of active pharmaceutical constituents into inorganic end-products.[57,64]
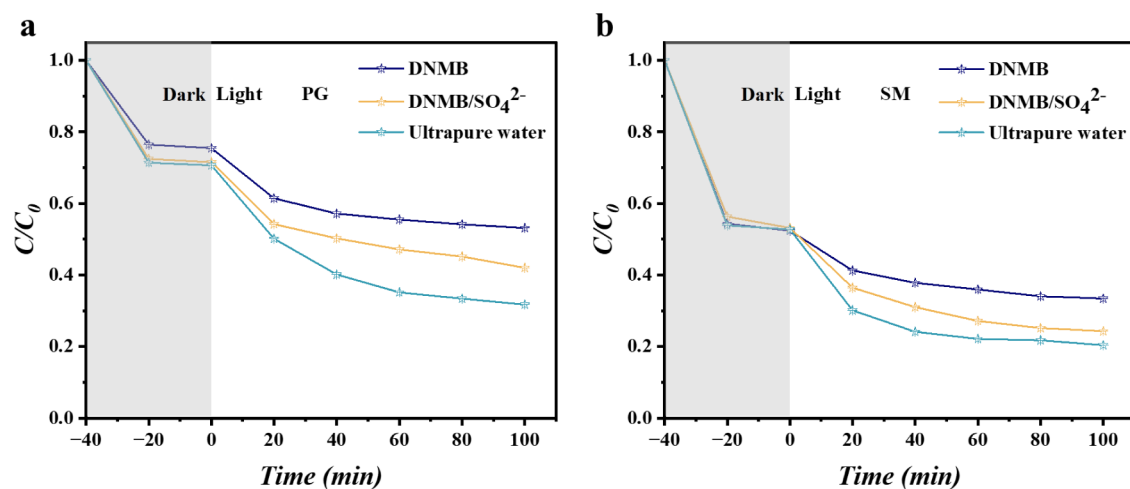
Figure 7. Photocatalytic degradation of (a) PG and (b) SM by DNMB/SO$_4^{2-}$ in actual biological wastewater. Na$_2$SO$_4$ concentration 10 mg L^{-1}.

For BPA, computational analysis identified C3 (f$^+$ = 0.0661) and C12 (f$^+$ = 0.0649) as the most electrophilically reactive sites, while C3 (f^0 = 0.0601) and C14 (f^0 = 0.0576) exhibited maximum radical scavenging potential (Figure S23). These reactivity patterns govern two distinct degradation mechanisms (Figure S24). Pathway 1 initiates with hydroxyl group elimination from BPA, generating intermediate P1 (211 *m/z*). Subsequent cleavage of the C−C bond bridging the benzene ring and isopropyl group under electrophilic conditions converts the electron-rich aromatic system into 4-isopropylphenol (P2, 151 *m/z*). Via intramolecular dehydration, P2 isomerizes to 4-isopropenylphenol (P3, 119 *m/z*), which undergoes further structural rearrangement to yield P4 (103 *m/z*). Pathway 2 commences with hydroxylation-driven photo transformation of BPA, forming hydroxylated derivative P5 (243 *m/z*). Sequential dehydration and oxidative ring-opening reactions then produce quinone (P6, 241 *m/z*) and carboxylic acid (P7, 289 *m/z*) intermediates. These aromatic byproducts progressively degrade into low-molecular-weight species, exemplified by ring-opened intermediate P8 (115 *m/z*), before ultimate mineralization into inorganic end-products.[2,65]

For RhB, computational analysis identified C7 (f$^+$ = 0.074), C11 (f$^+$ = 0.0591), and C2 (f$^+$ = 0.0591) as the most electrophilically reactive sites, while N36 and N37 exhibited the highest radical scavenging capacity (f^0 = 0.0558 for both, Figure S25). Degradation primarily targets peripheral carbon chains through two mechanistic routes (Figure S26). Pathway 1 involves sequential N-demethylation reactions, generating isomeric intermediates P1 and P2 (415 *m/z*). Pathway 2 proceeds via hydroxylation to form oxidized derivative P3 (459 *m/z*), followed by ethylation and hydroxylation steps yielding P4/P5 (359 *m/z*) and P6 (379 *m/z*). Concurrently, chromene ring cleavage and oxidative ring-opening reactions produce aromatic fragments P9 (230 *m/z*) and aliphatic species P10 (85 *m/z*). Systematic degradation ultimately achieves complete fragmentation of the conjugated xanthene structure into low-molecular-weight mineralization products.[58,66]

The toxicity profiles of both parent pollutants and their degradation intermediates were assessed using the Toxicity Estimation Software Tool (T.E.S.T.), with evaluations encompassing mutagenicity, developmental toxicity, and rat oral LD50 (Figures S27−S31). Analytical data indicate that most degradation products exhibited reduced toxicity compared to the original contaminants. Although a minor fraction of intermediates displayed transiently elevated toxicity relative to their parent compounds, these effects were substantially diminished in subsequent degradation stages. These findings collectively demonstrate that the photocatalytic process achieves dual objectives: efficient pollutant degradation and mitigation of secondary contamination risks associated with toxic intermediates.

In summary, the reaction mechanism of the DNMB/SO$_4^{2-}$ system can be described as follows: upon exposure to visible light, photogenerated electrons and holes lead to the production of various reactive species, such as O$_2^-$, H$_2$O$_2$, ●OH and SO$_4^-$ (eqs 5−10).[52,53] Based on the calculations of HOMO, LUMO, and Fukui indices, the specific degradation sites of the pollutants can then be identified. The redox cycling between Fe^{2+} and Fe^{3+} in DNMB further facilitates these processes. In conventional MOF systems, the redox cycling is hindered due to the depletion of Fe^{2+}. However, the addition of SO$_4^{2-}$ promotes the reduction of Fe^{3+} to Fe^{2+} through the participation of photogenerated electrons, thereby sustaining the redox cycle.[15,67] The changes in metal valence states significantly enhance the production of reactive radicals while boosting the efficiency of the separation of electron−hole pairs. Compared to conventional degradation systems, the introduction of SO$_4^{2-}$ substantially enhances the photocatalytic degradation efficiency of organic pollutants. The strong nucleophilicity of sulfate radicals synergizes with hydroxyl radicals to target electron-deficient and electron-accepting sites. Moreover, the interplay between sulfate radicals and the intrinsic Fe^{3+}/Fe^{2+} redox cycles in DNMB ensures continuous electron transfer and maintains a high Fe^{2+} concentration, overcoming the limitations of conventional MOF systems where the Fe^{2+} levels rapidly decline. These unique advantages of the DNMB/SO$_4^{2-}$ system correlate well with the significant performance enhancement observed above.

Impacts of Solution Parameters. Based on the aforementioned mechanism, the impacts of solution conditions on the photocatalytic performance was further examined. From Figure S32, the degradation efficiency for the five pollutants by DNMB/SO$_4^{2-}$ can be found to reach a maximum mostly at slightly acidic/neutral pH.[68−72]

In natural water systems, the presence of other cations and anions may also affect the catalytic performance. From Figure S33, it can be observed that common cations (e.g., Na^+, K^+, NH_4^+, and Ca^{2+}) slightly reduced the photocatalytic degradation performance. For instance, after 100 min of irradiation, the efficiencies of TC degradation diminished from 92.6% to 74.2%, 61.5%, 62.5%, and 68.6% in the presence of Na^+, Ca^{2+}, K^+, and NH_4^+, respectively. Similarly, the degradation efficiencies decreased from 89.4% to 75.1%, 72.8%, 73.9%, and 68.2% for SMX, from 75.2% to 56.0%, 54.0%, 62.9%, and 59.1% for LEV, from 91.2% to 63.6%, 60.1%, 48.9%, and 71.5% for BPA, and from 94.7% to 80.1%, 78.2%, 76.3%, and 80.5% for RhB. Among these pollutants, BPA exhibited the most pronounced decline in degradation efficiency. Similarly, common anions such as Cl^- and others (Figure S33) showed a comparable diminishing trend of the degradation efficiency, likely because of interference of electrostatic interactions between the pollutant molecules and the catalysts (vide ante).

Application in Actual Biological Wastewater Treatment. The potential application of the $DNMB/SO_4^{2-}$ system was further evaluated using actual wastewater samples. Biological wastewater was obtained from the Institute of High Energy Physics, Chinese Academy of Sciences. The characteristics of the wastewater are summarized in Table S5, and penicillin G (PG) and streptomycin (SM) were selected as the target pollutants. As manifested in Figure 7, the degradation efficiencies of PG and SM in actual wastewater were ca. 46.9% and 66.6% after 40 min's visible light irradiation by DNMB alone, in comparison to 69.3% and 79.7% in ultrapure water. This was most likely ascribed to other organic compounds present in the wastewater that quenched the reactive radicals and hindered the degradation process. Nevertheless, upon the addition of Na_2SO_4 (10 mg L^{-1}) the degradation rate was markedly enhanced to 57.1% for PG and 72.4% for SM. This indicates that the addition of SO_4^{2-} can effectively mitigate the negative impacts of organic substances in actual wastewater on the pollutant removal, most likely due to the strong oxidizing property of SO_4^-.

Cycling Performance. Notably, DNMB exhibited excellent reusability. In six consecutive cycles, the degradation efficiency of the five contaminants showed only a slight decline (Figure S34a-e). XRD measurements (Figure S34f) confirmed that the structure of DNMB remained largely intact, indicating its high structural stability. XPS measurements of the Fe 2p electrons yielded consistent results in terms of the Fe^{2+}:Fe^{3+} atomic ratio and binding energies (Figure S35).

Photocatalyst Performance Comparison. Notably, in comparison to relevant catalysts described recently in the literature toward the photocatalytic degradation of pollutants, $DNMB/SO_4^{2-}$ was actually highly comparable to the best catalysts within the context of degradation efficiency and reaction time (Table S6), highlighting the unique potential of self-excited sulfate in photocatalysis.

CONCLUSION

In this study, NMB was prepared by a facile hydrothermal procedure, and defects were markedly enriched by adding potassium sodium tartrate during hydrothermal synthesis. The resultant DNMB exhibited improved photocatalytic activity toward the degradation of diverse organic pollutants, and the performance was further enhanced by the addition of sulfate anions, due to the formation of strongly oxidizing sulfate radicals that was facilitated by the Fe^{3+}/Fe^{2+} redox cycles. This was indeed validated by results from quenching experiments, ESR studies, theoretical calculations and LC-MS analyses, where the corresponding reaction pathways and mechanisms were proposed. Such a unique activity of the DNMB/sulfate system could be exploited for practical applications, as manifested in the effective degradation of organic pollutants in actual biological wastewater. These result underscore the critical impacts of structural engineering on advancing the development of green and sustainable environmental technologies.

ASSOCIATED CONTENT

Supporting Information

The Supporting Information is available free of charge at https://pubs.acs.org/doi/10.1021/acs.langmuir.5c01201.

Additional details of XPS studies; additional data of TEM, SEM, and XPS measurements; nitrogen sorption, photocurrent, photoluminescence, and contact angle analyses; HPLC-MS studies; computational results and reaction pathways; toxicity assessments; impacts of solution parameters; sample stability tests; and performance comparison (PDF)

AUTHOR INFORMATION

Corresponding Authors

Qiang Wang − Laboratory for Micro-sized Functional Materials & College of Elementary Education and Department of Chemistry, Capital Normal University, Beijing 100048, China; orcid.org/0000-0002-9118-5615; Email: qwchem@gmail.com

Shaowei Chen − Department of Chemistry and Biochemistry, University of California, Santa Cruz, California 95064, United States; orcid.org/0000-0002-3668-8551; Email: shaowei@ucsc.edu

Authors

Zeping Qin − Laboratory for Micro-sized Functional Materials & College of Elementary Education and Department of Chemistry, Capital Normal University, Beijing 100048, China

Mingming Sun − Laboratory for Micro-sized Functional Materials & College of Elementary Education and Department of Chemistry, Capital Normal University, Beijing 100048, China

Runjie Wu − Laboratory for Micro-sized Functional Materials & College of Elementary Education and Department of Chemistry, Capital Normal University, Beijing 100048, China

Pengkun Li − Laboratory for Micro-sized Functional Materials & College of Elementary Education and Department of Chemistry, Capital Normal University, Beijing 100048, China

Ran Tai − Laboratory for Micro-sized Functional Materials & College of Elementary Education and Department of Chemistry, Capital Normal University, Beijing 100048, China

Hongfei Su − Laboratory for Micro-sized Functional Materials & College of Elementary Education and Department of Chemistry, Capital Normal University, Beijing 100048, China

John Tressel − *Department of Chemistry and Biochemistry, University of California, Santa Cruz, California 95064, United States*

Bicheng Ji − *Beijing Key Laboratory of Functional Materials for Building Structure and Environment Remediation, Beijing University of Civil Engineering and Architecture, Beijing 100044, China*

Complete contact information is available at:
https://pubs.acs.org/10.1021/acs.langmuir.5c01201

Notes
The authors declare no competing financial interest.

ABBREVIATIONS

NMB	NH_2-MIL-88B
DNMB	defective NH_2-MIL-88B
TC	tetracycline
SMX	sulfamethoxazole
BPA	bisphenol A
RHB	rhodamine B
LEV	levofloxacin
PG	penicillin
SM	streptomycin

REFERENCES

(1) Lee, J.; Kim, J. Heterostructured photocatalytic fabric composed of Ag_3PO_4 nanoparticle-decorated NH_2-MIL-88B (Co/Fe) crystalline wires for Rhodamine B adsorption and degradation. *ACS Appl. Nano Mater.* **2024**, 7 (7), 8362−8375.

(2) Zhang, M.; Cao, H.; Wu, M.; Zhang, Y.; Zhu, J.; Xu, J.; Deng, J.; Zhou, T. Rational fabrication of Z-scheme heterojunction $ZnFe_2O_4$-seed@TpTt-COF for the visible-light-driven photocatalytic degradation of bisphenol A in food waste leachate boosted by primitive humic acid. *Chem. Eng. J.* **2024**, 487, 150684.

(3) Kaur, M.; Mehta, S. K.; Devi, P.; Kansal, S. K. Bi_2WO_6/NH_2-MIL-88B(Fe) heterostructure: an efficient sunlight driven photocatalyst for the degradation of antibiotic tetracycline in aqueous medium. *Adv. Powder Technol.* **2021**, 32 (12), 4788−4804.

(4) Ghamarpoor, R.; Jamshidi, M.; Fallah, A.; Eftekharipour, F. Preparation of dual-use GPTES@ZnO photocatalyst from waste warm filter cake and evaluation of its synergic photocatalytic degradation for air-water purification. *J. Environ. Manage.* **2023**, 342, 118352.

(5) Wu, Y.; Cai, W.; Zhong, S.; Lin, C.; Lin, M.; Lin, T.; Gao, M.; Zhao, C.; Wu, X. Sustainable NH_2-MIL-88B(Fe)/agarose carbon aerogel as a photo-Fenton catalyst for ultrafast degrading mitoxantrone. *J. Environ. Chem. Eng.* **2024**, 12 (4), 113155.

(6) Zhang, Z.; Bai, Z.; Yu, S.; Meng, X.; Xiao, S. Photo-Fenton efficient degradation of organic pollutants over S-scheme ZnO@NH_2-MIL-88B heterojunction established for electron transfer channel. *Chem. Eng. Sci.* **2024**, 288, 119789.

(7) Ghamarpoor, R.; Jamshidi, M.; Kandelousi, D. M. Electromagnetic Interference (EMI) shielding, electrical, thermal, and mechanical properties of silanized hexagonal boron nitride (h-BN) heterostructures and decorated by Ag nanoparticles: Towards smart coatings. *J. Alloys Compd.* **2025**, 1020, 179561.

(8) Yan, X.; Dong, J.-H.; Zheng, J.-Y.; Wu, Y.; Xiao, F.-X. Customizing precise, tunable, and universal cascade charge transfer chains towards versatile photoredox catalysis. *Chem. Sci.* **2024**, 15 (8), 2898−2913.

(9) Bai, X.; Liu, X.; Zong, R. Enhancement of Photocatalytic Self-Fenton Degradation toward Sulfamethoxazole by Highly Symmetrical Triazine-based Covalent Organic Frameworks. *Appl. Catal. B Environ. Energy* **2025**, 366, 125062.

(10) Hu, X.; Bao, J.; Chen, D.; Shah, S. J.; Subhan, S.; Gong, W.; Li, W.; Luan, X.; Zhao, Z.; Zhao, Z. Accelerating the Fe(III)/Fe(II) cycle via enhanced electronic effect in NH_2-MIL-88B(Fe)/TPB-DMTP-COF composite for boosting photo-Fenton degradation of sulfamerazine. *J. Colloid Interface Sci.* **2022**, 624, 121−136.

(11) Liang, H.; Liu, B.-J.; Tang, B.; Zhu, S.-C.; Li, S.; Ge, X.-Z.; Li, J.-L.; Zhu, J.-R.; Xiao, F.-X. Atomically Precise Metal Nanocluster-Mediated Photocatalysis. *ACS Catal.* **2022**, 12 (7), 4216−4226.

(12) Ning, B.; Chen, Z.; Cai, Y.; Xiao, F.-X.; Xu, P.; Xiao, G.; He, Y.; Zhan, L.; Zhang, J. Simultaneous Photocatalytic Tetracycline Oxidation and Cr(VI) Reduction by Z-Scheme Multiple Layer TiO_2/$SnIn_4S_8$. *Langmuir* **2024**, 40 (17), 9144−9154.

(13) Mo, Q.-L.; Xiong, R.; Dong, J.-H.; Sa, B.-S.; Zheng, J.-Y.; Chen, Q.; Wu, Y.; Xiao, F.-X. Identification of origin of insulating polymer maneuvered photoredox catalysis. *Chin. J. Catal.* **2024**, 63, 109−123.

(14) Chen, Z.; Li, G.; Zheng, X.; Liu, Y.; Dai, J.; Huang, B.; Xia, M.; Yan, L.; Chen, Q.; Shen, Y.; Wang, D.; Li, M.; Xiao, W.; Tian, X.; Xiao, J. Facile synthesis of advanced $BaTiO_3$/$CuPbSbS_3$ heterostructure photocatalyst with enhanced piezo-photocatalytic degradation performance. *Nano Energy* **2024**, 124, 109463.

(15) Sun, K.; Wang, X.; Yuan, H.; Hou, J.; Shi, W.; Li, C.; Guo, F. Magnetically separable and recyclable $ZnFe_2O_4$ nanoparticles as an effective activator in resorcinol-formaldehyde resins-based photocatalysis-self-Fenton system. *Sep. Purif. Technol.* **2024**, 351, 128044.

(16) Dhillon, M.; Moitra, T.; Dhingra, S.; Kailasam, K.; Chakraborty, B.; Basu, A. K. Resilient 3D printed porous biodegradable Polylactic Acid coated with Bismuth Ferrite for Piezo Enhanced Photocatalysis degradation assisted by Machine Learning. *Nano Energy* **2025**, 140, 111010.

(17) Liu, Z.; Liu, Y.; Sun, X.; Ji, H.; Liu, W.; Cai, Z. Construction of Z-scheme Ag/$AgVO_3$/carbon-rich g-C_3N_4 heterojunction for enhanced photocatalytic degradation of sulfamethiadiazole: DFT calculation and mechanism study. *Chem. Eng. J.* **2022**, 433, 133604.

(18) Chata, G.; Nichols, F.; Mercado, R.; Assafa, T.; Millhauser, G. L.; Saltikov, C.; Chen, S. W. Photodynamic Activity of Graphene Oxide/Polyaniline/Manganese Oxide Ternary Composites Towards Both Gram-Positive and Gram-Negative Bacteria. *ACS Appl. Bio Mater.* **2021**, 4, 7025−7033.

(19) Zhang, G.-Y.; Wang, J.-J.; Shen, X.-Q.; Wang, J.-J.; Wang, B.-Y.; Gao, D.-Z. Br-doped $Bi_2O_2CO_3$ nanosheets with improved electronic structure and accelerated charge migration for outstanding photocatalytic behavior. *Appl. Surf. Sci.* **2019**, 470, 63−73.

(20) Zhang, C.; Hu, S.; Cui, W.; Li, S.; Tian, L.; Yuan, X.; Tariq, W.; Yao, K.; Zhi, Y.; Hu, T.; Shan, S. Integrating photocatalytic hydrogen evolution with antibiotic degradation over a dual Z-scheme heterojunction. *Chem. Eng. J.* **2025**, 510, 160317.

(21) Liu, Z.; Hao, W.; Yuan, C.; Ruan, W.; Jiang, W.; Teng, F. Substantially updating photocatalytic reaction by in-situ generated SO_4^- through directly exciting SO_4^{2-}. *J. Water Process. Eng.* **2022**, 48, 102912.

(22) Meng, H.; Zhou, J.; Zhang, Y.; Cui, J.; Chen, Y.; Zhong, W.; Chen, Y.; Jia, C. Q. Single-atom Co-N_3 sites induce peroxymonosulfate activation for acetaminophen degradation via nearly 100% internal electron transfer process. *Appl. Catal. B Environ. Energy* **2025**, 366, 125038.

(23) Ren, S.; Wang, Y.; Shi, L.; Xu, X.; Zhong, S.; Hu, K.; Zhou, H.; Zhu, Z.-S.; Zhou, P.; Tian, W.; et al. Transforming Plastics to Single Atom Catalysts for Peroxymonosulfate Activation: Axial Chloride Coordination Intensified Electron Transfer Pathway. *Adv. Mater.* **2025**, 37 (8), 2415339.

(24) Shan, C.; Xu, Y.; Hua, M.; Gu, M.; Yang, Z.; Wang, P.; Lu, Z.; Zhang, W.; Pan, B. Mesoporous Ce-Ti-Zr ternary oxide millispheres

for efficient catalytic ozonation in bubble column. *Chem. Eng. J.* **2018**, *338*, 261−270.

(25) Lee, J.; Kim, J. Cooperative design of the Ag$_3$PO$_4$/NH$_2$-MIL-88B (Fe/Co) heterojunction integrated with conductive polypyrrole for advanced photocatalytic water purification. *ACS Omega* **2024**, *9* (5), 5942−5953.

(26) He, H.; Wang, Y.; Li, J.; Jiang, S.; Sidra, S.; Gong, W.; Tang, Y.; Hu, Y.; Wei, R.; Yang, D.; Li, X.; Zhao, Z. Confined conductive and light-adsorbed network in metal organic frameworks (MIL-88B(Fe)) with enhanced photo-Fenton catalytic activity for sulfamethoxazole degradation. *Chem. Eng. J.* **2022**, *427*, 131962.

(27) Tai, R.; Gao, S.; Tang, Y.; Ma, X.; Ding, P.; Wu, R.; Li, P.; Song, X.; Chen, S.; Wang, Q. Defect engineering of Bi$_2$WO$_6$ for enhanced photocatalytic degradation of antibiotic pollutants. *Small* **2024**, *20* (29), 2310785.

(28) Zhu, A.; Liu, P.; Wang, Z.; Liu, Z.; Liu, A.; Guan, L. Visible photocatalytic degradation of tetrabromobisphenol A by CuO-modified Ce$_2$O$_3$: Mechanisms and DFT studies. *J. Environ. Chem. Eng.* **2022**, *10* (6), 108878.

(29) Li, Y.-H.; Wang, C.-C.; Wang, F.; Liu, W.; Chen, L.; Zhao, C.; Fu, H.; Wang, P.; Duan, X. Nearly zero peroxydisulfate consumption for persistent aqueous organic pollutants degradation via nonradical processes supported by in-situ sulfate radical regeneration in defective MIL-88B(Fe). *Appl. Catal., B* **2023**, *331*, 122699.

(30) Zheng, X.; Shen, Y.; Zhou, Y.; Wen, H.; Wen, J. Solar-light induced photocatalytic-persulfate activity of BiOCl$_{0.5}$I$_{0.5}$/NH$_2$-MIL-88B(Fe) for tetracycline hydrochloride degradation. *J. Water Process. Eng.* **2023**, *54*, 104034.

(31) Choi, S.; Kim, T.; Ji, H.; Lee, H. J.; Oh, M. Isotropic and anisotropic growth of metal−organic framework (MOF) on MOF: logical inference on MOF structure based on growth behavior and morphological feature. *J. Am. Chem. Soc.* **2016**, *138* (43), 14434−14440.

(32) Bao, J.; Zhang, H.; Muhammad, Y.; Wei, H.; Wang, R.; Fang, G.; Zhao, Z.; Zhao, Z. Oriented anchoring of NCQD on citric acid defective cluster of NH$_2$-MIL-88B(Fe) for the efficient removal of tetracycline via photo-Fenton catalysis. *Chem. Eng. J.* **2023**, *456*, 141063.

(33) Zhong, X.; Xu, J.; Song, S. Synergistic effects in simultaneous photocatalytic removal of Cr(VI) and As(III) by bimetallic NH$_2$-MOF(InxFe1−x). *Appl. Surf. Sci.* **2025**, *690*, 162659.

(34) Zhao, K.; Zhang, Z.; Feng, Y.; Lin, S.; Li, H.; Gao, X. Surface oxygen vacancy modified Bi$_2$MoO$_6$/MIL-88B(Fe) heterostructure with enhanced spatial charge separation at the bulk & interface. *Appl. Catal., B* **2020**, *268*, 118740.

(35) Jiang, Z.; Wang, L.; Lei, J.; Liu, Y.; Zhang, J. Photo-Fenton degradation of phenol by CdS/rGO/Fe^{2+} at natural pH with in situ-generated H$_2$O$_2$. *Appl. Catal., B* **2019**, *241*, 367−374.

(36) Wu, R.; Gao, S.; Jones, C.; Sun, M.; Guo, M.; Tai, R.; Chen, S.; Wang, Q. Bi/BSO heterojunctions via vacancy engineering for efficient photocatalytic nitrogen fixation. *Adv. Funct. Mater.* **2024**, *34* (24), 2314051.

(37) Zhang, S.; Zhuo, Y.; Ezugwu, C. I.; Wang, C.-C.; Li, C.; Liu, S. Synergetic molecular oxygen activation and catalytic oxidation of formaldehyde over defective MIL-88B(Fe) nanorods at room temperature. *Environ. Sci. Technol.* **2021**, *55* (12), 8341−8350.

(38) Surblé, S.; Serre, C.; Mellot-Draznieks, C.; Millange, F.; Férey, G. A new isoreticular class of metal-organic-frameworks with the MIL-88 topology. *Chem. Commun.* **2006**, *3*, 284−286.

(39) Huang, W.; Jing, C.; Zhang, X.; Tang, M.; Tang, L.; Wu, M.; Liu, N. Integration of plasmonic effect into spindle-shaped MIL-88A(Fe): Steering charge flow for enhanced visible-light photocatalytic degradation of ibuprofen. *Chem. Eng. J.* **2018**, *349*, 603−612.

(40) Yang, S.; Wang, X.; Song, G.; Lu, G.; Shi, G.; Wang, Y.; Xie, X.; Sun, J. Ti-O-Mo bond-bridged PMA@MIL-125-NH$_2$ photocatalyst for gas acetone photocatalytic degradation. *Appl. Catal. B Environ. Energy* **2025**, *367*, 125112.

(41) Yadav, H. M.; Kim, J.-S. Fabrication of SiO$_2$/TiO$_2$ double layer thin films with self-cleaning and photocatalytic properties. *J. Mater. Sci.: Mater. Electron.* **2016**, *27* (10), 10082−10088.

(42) Shan, Y.; Zhang, G.; Shi, Y.; Pang, H. Synthesis and catalytic application of defective MOF materials. *Cell Rep. Phys. Sci.* **2023**, *4* (3), 101301.

(43) Taha, S.; Amer, M.; Elmarsafy, A.; Elkady, M.; Chovelon, J.-M. Degradation of boscalid by nitrogen-doped/undoped TiO2 and persulfate ions using different activation conditions and the identification of its main degradation products using LC/MS/MS. *Chem. Eng. J.* **2016**, *288*, 845−857.

(44) Lei, Y.; Yu, Y.; Lei, X.; Liang, X.; Cheng, S.; Ouyang, G.; Yang, X. Assessing the Use of Probes and Quenchers for Understanding the Reactive Species in Advanced Oxidation Processes. *Environ. Sci. Technol.* **2023**, *57* (13), 5433−5444.

(45) Wang, X.; Du, Y.; Liu, H.; Ma, J. Ascorbic acid/Fe0 composites as an effective persulfate activator for improving the degradation of rhodamine B. *RSC Adv.* **2018**, *8* (23), 12791−12798.

(46) Nichols, F.; Chen, S. Graphene Oxide Quantum Dot-Based Functional Nanomaterials for Effective Antimicrobial Applications. *Chem. Rec.* **2020**, *20* (12), 1505−1515.

(47) Sun, L.; Sun, Q.; He, Y.; Feng, J.; Gan, Z.; Yu, L.; Dong, L. Rapid and deep photocatalytic degradation of polyvinyl alcohol by black phosphorus quantum dot sensitized g-C$_3$N$_4$. *Chem. Eng. J.* **2023**, *473*, 145367.

(48) Guan, Z.; Li, X.; Wu, Y.; Chen, Z.; Huang, X.; Wang, D.; Yang, Q.; Liu, J.; Tian, S.; Chen, X.; Zhao, H. AgBr nanoparticles decorated 2D/2D GO/Bi$_2$WO$_6$ photocatalyst with enhanced photocatalytic performance for the removal of tetracycline hydrochloride. *Chem. Eng. J.* **2021**, *410*, 128283.

(49) Li, W.-Q.; Savateev, O.; Li, Y.-M.; Zheng, J.-K.; Wang, Y.-X.; Hou, N.; Liu, X.-C.; Ding, R.-R.; Zhou, X.-G.; Wang, Y.; Shi, X.-Y.; Mu, Y. Boosting persulfate activation through efficient $\pi \rightarrow \pi^*$ transition activated by Cu ion anchored porphyrin-based metal−organic framework. *Chem. Eng. J.* **2024**, *490*, 151802.

(50) Jia, Y.; Li, H.; Duan, L.; Gao, Q.; Zhang, H.; Li, S.; Li, M. Activation of persulfate by β-PDI/MIL-101(Fe) photocatalyst under visible light toward efficient degradation of sulfamethoxazole. *Chem. Eng. J.* **2024**, *481*, 148588.

(51) Yuan, R.; Yue, C.; Qiu, J.; Liu, F.; Li, A. Highly efficient sunlight-driven reduction of Cr(VI) by TiO$_2$@NH$_2$-MIL-88B(Fe) heterostructures under neutral conditions. *Appl. Catal., B* **2019**, *251*, 229−239.

(52) Zhang, Q.; Qu, G.; Wang, T.; Li, C.; Qiang, H.; Sun, Q.; Liang, D.; Hu, S. Humic acid removal from micro-polluted source water in the presence of inorganic salts in a gas-phase surface discharge plasma system. *Sep. Purif. Technol.* **2017**, *187*, 334−342.

(53) Yang, Y.; Jiang, J.; Lu, X.; Ma, J.; Liu, Y. Production of Sulfate Radical and Hydroxyl Radical by Reaction of Ozone with Peroxymonosulfate: A Novel Advanced Oxidation Process. *Environ. Sci. Technol.* **2015**, *49* (12), 7330−7339.

(54) Ji, H.; Du, P.; Zhao, D.; Li, S.; Sun, F.; Duin, E. C.; Liu, W. 2D/1D graphitic carbon nitride/titanate nanotubes heterostructure for efficient photocatalysis of sulfamethazine under solar light: Catalytic "hot spots" at the rutile−anatase−titanate interfaces. *Appl. Catal., B* **2020**, *263*, 118357.

(55) Ni, Q.; Ke, X.; Qian, W.; Yan, Z.; Luan, J.; Liu, W. Insight into tetracycline photocatalytic degradation mechanism in a wide pH range on BiOI/BiOBr: Coupling DFT/QSAR simulations with experiments. *Appl. Catal., B* **2024**, *340*, 123226.

(56) Chen, Y.; Li, R.; Gu, T.; Zhang, W.-X. Effective periodate activation by the ball-milled bimetallic zero-valent iron/manganese oxides catalyst for sulfamethoxazole degradation. *Chem. Eng. J.* **2024**, *500*, 156967.

(57) Zhang, C.; Lin, L.; Zhou, M.; Wang, Y.; Xu, S.; Chen, X.; Li, Z. Dual functional S-scheme ZnIn$_2$S$_4$/crystalline polymeric carbon nitride (ZIS/CPCN) heterojunction for efficient photocatalytic hydrogen evolution and degradation of levofloxacin. *Chem. Eng. J.* **2024**, *495*, 153563.

(58) Jiang, X.; Sun, S.; Wang, Y.; Zhao, L.; Huang, F.; Li, S. Design of interfacial dual Schottky junctions to modulate charge transfer for enhanced piezo-assisted photocatalytic degradation RhB performances. *J. Mater. Chem. A* **2024**, *12* (20), 12146−12154.

(59) Mehmood, A.; Jones, S. I.; Tao, P.; Janesko, B. G. An orbital-overlap complement to ligand and binding site electrostatic potential maps. *J. Chem. Inf. Model.* **2018**, *58* (9), 1836−1846.

(60) Li, Q.; Zhou, H.; Li, Z.; Liu, A.; Wang, E.; Wu, Y.; Tang, X.; Du, H.; Jin, L.; Zhu, H.; Ni, B.; Wang, W. Efficient photocatalytic degradation of antibiotics using Z-scheme MIL-88(Fe)/Ti_3C_2/MoO_3: Mechanistic insights and toxicity assessment. *J. Hazard. Mater.* **2025**, *486*, 137051.

(61) Wang, S.-H.; Du, M.; Guo, H.-L.; Chen, H.-Y.; Pang, J.-Y.; Dang, D.-B.; Bai, Y. Carboxylate-functionalized polyoxo-titanium clusters for adsorption/solar photocatalytic synergistic tetracycline degradation. *J. Mater. Chem. A* **2025**, *13* (8), 5860−5869.

(62) Ju, Y.; Lin, H.; Chen, C.; Hou, R.; Wang, Z.; Hao, T.; Xu, M.; Tang, Y.; Chen, F. Two-Level regulation photocatalytic activity of Bi_2WO_6/COFs with ligand engineering and piezoelectric field for Highly-Efficient degradation of antibiotics. *Chem. Eng. J.* **2024**, *498*, 155790.

(63) Shi, L.; Li, Y.; Dong, H.; Sun, J.; Xia, C.; Cai, L.; Hui, B. Heterostructural Cu_2S@CuO nanoarrays enable peroxymonosulfate activation for sulfamethoxazole degradation through non-free radical pathways. *Desalination* **2025**, *600*, 118527.

(64) Trifoglio, A.; Tunioli, F.; Favaretto, L.; Zambianchi, M.; Bettini, C.; Manet, I.; Mariani, L.; Barra Caracciolo, A.; Grenni, P.; Di Sante, M.; Di Giosia, M.; Marforio, T. D.; Mattioli, E. J.; Calvaresi, M.; Melucci, M. Alginate−oligothiophene aerogels as photocatalysts for the degradation of emerging organic contaminants in water. *J. Mater. Chem. A* **2025**, *13*, 4587−4599.

(65) Yan, J.; Zhang, J.; Wang, Y.; Lv, J.; Zhang, H.; Tong, Z.; Yu, Y.; Liu, K. Visible light-driven selective oxidation of multiple organic matters by photocatalysis of BiOX (X = I, Br): New insights into the role of oxygen vacancy generation and electron gain/loss properties of matter. *Sep. Purif. Technol.* **2025**, *361*, 131486.

(66) Chai, M.; Xing, R.-J.; Chen, J.; Su, Z.-X.; Wei, H.; Zhu, H.-W.; Gong, X.-Q. Atomic Pd Sites on CeO_2 Nanorods for Highly Selective Hydrogen Peroxide Generation and Efficient Degradation of Organic Pollutants. *ACS Sustainable Chem. Eng.* **2025**, *13* (3), 1391−1400.

(67) Shi, W.; Liu, Y.; Sun, W.; Hong, Y.; Li, X.; Lin, X.; Guo, F.; Shi, J. Improvement of synergistic effect photocatalytic/peroxymonosulfate activation for degradation of amoxicillin using carbon dots anchored on rod-like $CoFe_2O_4$. *Chin. J. Chem. Eng.* **2022**, *52*, 136−145.

(68) Saadati, F.; Keramati, N.; Ghazi, M. M. Influence of parameters on the photocatalytic degradation of tetracycline in wastewater: A review. *Crit. Rev. Environ. Sci. Technol.* **2016**, *46* (8), 757−782.

(69) Manju, R.; Samraj, J. J.; Neppolian, B. Real sample analysis of persistent contaminant abatement via synergistic adsorption and visible-light catalysis in continuous flow reactors. *Sep. Purif. Technol.* **2025**, *360*, 131050.

(70) Mzimela, N.; Tichapondwa, S.; Chirwa, E. Visible-light-activated photocatalytic degradation of rhodamine B using WO3 nanoparticles. *RSC Adv.* **2022**, *12* (53), 34652−34659.

(71) Sharma, S.; Umar, A.; Mehta, S. K.; Ibhadon, A. O.; Kansal, S. K. Solar light driven photocatalytic degradation of levofloxacin using TiO2/carbon-dot nanocomposites. *New J. Chem.* **2018**, *42* (9), 7445−7456.

(72) Liu, B.; Qiao, M.; Wang, Y.; Wang, L.; Gong, Y.; Guo, T.; Zhao, X. Persulfate enhanced photocatalytic degradation of bisphenol A by g-C_3N_4 nanosheets under visible light irradiation. *Chemosphere* **2017**, *189*, 115−122.